Energy & Environmental Science

ROYAL SOCIETY OF CHEMISTRY

PAPER

View Article Online
View Journal | View Issue

Check for updates

Cite this: *Energy Environ. Sci.*, 2024, **17**, 190

A weakly ion pairing electrolyte designed for high voltage magnesium batteries†

Chang Li,[ab] Rishabh D. Guha,[c] Abhinandan Shyamsunder,[ab] Kristin A. Persson*[bde] and Linda F. Nazar*[ab]

Received 28th August 2023,
Accepted 14th November 2023

DOI: 10.1039/d3ee02861e

rsc.li/ees

Published on 16 November 2023. Downloaded on 8/23/2025 1:21:11 PM.

High-voltage rechargeable magnesium batteries (RMBs) are potential alternatives to lithium-ion batteries owing to the low cost and high abundance of magnesium. However, the parasitic reactions of the latter with many electrolytes greatly hinders the stability and kinetics of Mg plating/stripping. Here we report a new and easily accessible solvent-designed electrolyte, which effectively solves the difficulty of ion pair dissociation and facilitates fast nanoscale Mg nucleation/growth using simple $Mg(TFSI)_2$ as the salt, enabling a facile interfacial charge transfer process. Dendrite-free Mg plating/stripping is maintained for over 7000 hours (~10 months) at a practical areal capacity of 2 mA h cm^{-2}. The high-voltage stability of these electrolytes is demonstrated by benchmarking with polyaniline||Mg full cells with an operating voltage up to 3.5 V that exhibit stable cycling at a 2C rate with 99% coulombic efficiency after 400 cycles. This work opens up new frontiers in coupling low-cost electrolytes with next-generation high-voltage cathode materials for fast-charging RMBs with long life and high energy densities.

Broader context

Net-zero carbon dioxide emission demands clean renewable energy, while harnessing it requires electrochemical storage devices with high energy density, safety and affordability. Rechargeable magnesium batteries (RMBs) are candidates because of the abundance of Mg (over 1000 times that of Li), the high theoretical volumetric energy density of Mg metal, and magnesium's low reduction potential. However, to date, there is no practical RMB on the market owing to many unsolved major challenges. The key factors can be partly addressed by designing better electrolytes. Here, we report a new concept for an electrolyte system that disrupts strong ion-pairing in solution, enabling highly reversible, high-voltage Mg metal batteries. This electrolyte relies on two key components: ethyl phosphate as a high dielectric solvent to unlock the activity of Mg^{2+}/Mg redox, and co-ether solvents to improve the kinetics and stability of Mg plating/stripping. The complex interactions between cation, anion and solvent are revealed by advanced spectroscopies and MD simulations, providing new design principles. The use of cost-effective and commercially available Mg salts simplifies scalability. The 4 V stability of this electrolyte is demonstrated by benchmarking Mg metal batteries assembled with an organic polymer cathode that run at a 2C rate for over 400 cycles with 99% coulombic efficiency up to 3.5 V. Our design opens up new frontiers for low-cost and high-voltage electrolyte approaches that take advantage of facile desolvation processes at the interfaces, and can establish a platform for new avenues of investigation for next generation energy storage in RMBs.

Introduction

Net-zero carbon dioxide emission demands clean renewable energy, while harnessing it requires electrochemical storage devices with high energy density, safety and affordability.[1–3] To achieve decarbonization, much effort is being devoted to new battery technologies beyond lithium-ion batteries (LIBs).[2,4] Rechargeable magnesium batteries (RMBs) stand out because of the abundance of Mg (over 1000 times that of Li),[5] the high theoretical volumetric energy density of a Mg metal anode (3833 mA h cm^{-3} *vs.* 2046 mA h cm^{-3} of Li),[6] and magnesium's relatively low reduction potential −2.38 V *versus* the standard hydrogen electrode (SHE)). Although Mg dendrite formation was confirmed in some studies,[7,8] generally Mg is thought to be less prone to this phenomenon[1] than Li,[9] and suggests RMBs

[a] *Department of Chemistry and the Waterloo Institute for Nanotechnology, University of Waterloo, Ontario N2L 3G1, Canada. E-mail: lfnazar@uwaterloo.ca*
[b] *Joint Center for Energy Storage Research, Argonne National Laboratory, Lemont, Illinois 60439, USA*
[c] *Materials Science Division, Lawrence Berkeley National Laboratory, Berkeley, California 94720, USA*
[d] *Molecular Foundry, Lawrence Berkeley National Laboratory, 1 Cyclotron Road, Berkeley, California 94720, USA. E-mail: kristinpersson@berkeley.edu*
[e] *Department of Materials Science and Engineering, UC Berkeley, Berkeley, California 94720, USA*

† Electronic supplementary information (ESI) available. See DOI: https://doi.org/10.1039/d3ee02861e

This journal is © The Royal Society of Chemistry 2024

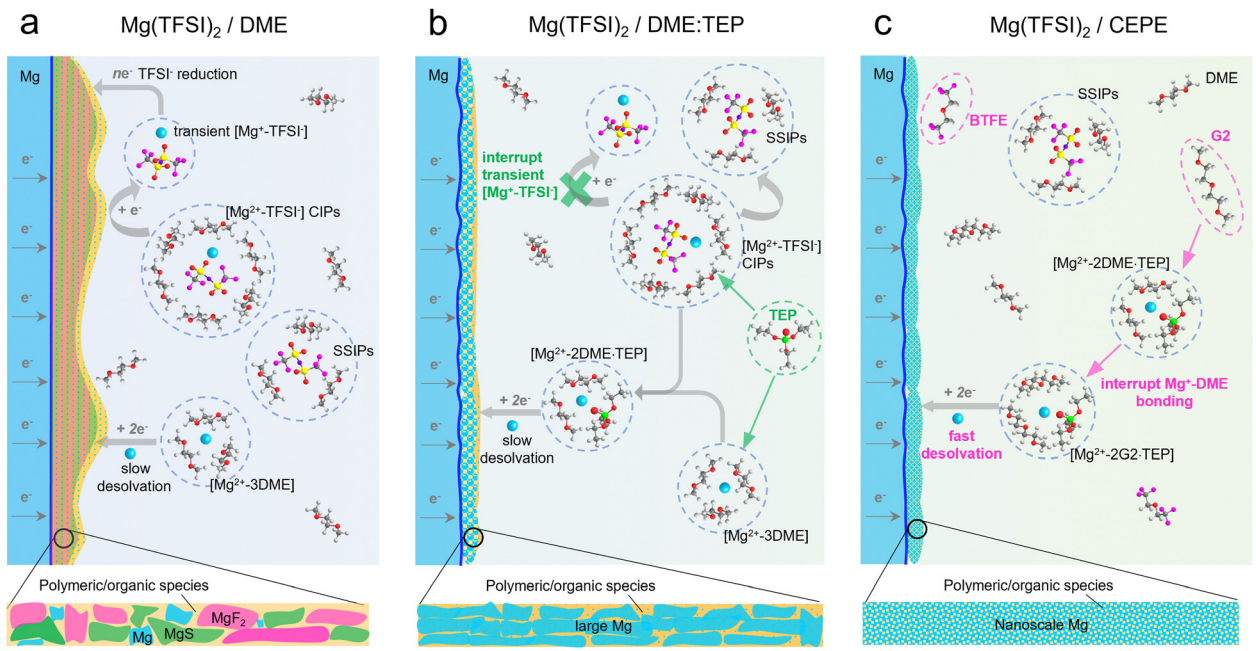
Published on 16 November 2023. Downloaded on 8/23/2025 1:21:11 PM.

can potentially be safer electrochemical energy devices than lithium metal batteries.[10]

Among many unaddressed challenges for practical RMBs, designing better electrolytes is one key to their successful commercialization.[1,4,5,11] The charge-dense Mg^{2+} cation results in: (1) a high desolvation penalty due to the slow kinetics of ion pair dissociation; and (2) very slow ion migration kinetics because of a thick solid electrolyte interface (SEI) on the Mg surface which impedes the interfacial charge transfer process.[1,12] Therefore, transferring electrolyte design principles from LIBs directly to RMBs is not possible. Utilizing conventional carbonate-based solvents and fluorinated anions such as BF_4^- and PF_6^- results in tightly bonded contact ion pairs (CIPs) that aggravate passivation of the Mg anode *via* pronounced electrolyte decomposition.[12] Classical Mg electrolytes rely on concentrated chloride species to unlock reversible Mg plating/stripping;[13] however, the latter are oxidatively unstable ($\sim$2.5 V *vs.* Mg^{2+}/Mg) and highly corrosive to current collectors or battery casings.[1] Their dominant intercalation species – $Mg_xCl_y^+$ – also lowers the energy density compared to Mg^{2+} storage.[11,14]

To tackle these challenges, halide-free Mg salts with bulky alkoxyborate/aluminate or carborane anions were developed that show high reversibility for Mg plating/stripping with over 99% coulombic efficiency (CE) and oxidative stability over 3.5 V *vs.* Mg^{2+}/Mg.[15–19] Among these, $Mg(CB_{11}H_{12})_2$ in a 1,2-dimethoxyethane (DME)/diglyme (G2) solvent blend exhibits very fast Mg plating/stripping, and can support 5C-rate cycling with pyrene-4,5,9,10-tetraone (PTO) as the enolization cathode.[20] The discovery of such bulky anion-salts dates back three decades.[12,21] Unfortunately, most are expensive due to the reagents needed for their complex synthesis and purification procedures, where trace impurities can cause short lifetimes for Mg plating/stripping.[11,16,22–24] A more economical option relies on modifying Mg electrolytes and using commercial halide-free salts such as magnesium bis(trifluoromethanesulfonimide) ($Mg(TFSI)_2$) with high oxidative stability (approaching 4 V *vs.* Mg^{2+}/Mg) and good ionic conductivity (1–6 mS cm^{-1}).[25–27] However, unlike bulky alkoxyborates/aluminates and carborane anions that prefer to exist as solvent-separated ion pairs (SSIPs) in ether-type solvents, the more electron localized $TFSI^-$ anion contributes to large fractions of CIPs that are easily reduced during Mg plating (Scheme 1(a)).[28–31] The resulting inorganic products (for example, MgF_2 and MgS), together with other solvent-derived polymeric/organic species,[32] lead to a thick impedance layer on the Mg surface that passivates Mg^{2+}/Mg charge transfer. Currently, only a few studies have shown reversible Mg plating/stripping in such electrolytes. Impressively, additives with high donor numbers – methoxyethylamines – that tightly coordinate with Mg^{2+} can suppress DME decomposition and enable efficient Mg plating/stripping with over 99.5% CE over 100 cycles.[33] Similarly, trimethyl phosphate was utilized to suppress DME decomposition.[34,35] However, $TFSI^-$ anion decomposition occurs in the latter, leading to a lifetime of $\sim$450 hours in symmetric cells at a current density of 0.1 mA cm^{-2}.[34,35] Nonetheless, the phosphate approach inspired us to design solvents to boost Mg anode stability.

Here, we invent a new co-ether phosphate electrolyte (CEPE) system that enables fast and highly stable Mg^{2+}/Mg redox



Scheme 1 Electrolyte design principles. (a) In a conventional $Mg(TFSI)_2$/DME electrolyte, the high content of CIPs leads to the formation of transient $[Mg^+–TFSI^-]$ clusters which are easily reduced during Mg plating. This results in a thick passivation layer consisting of inorganic MgF_2, MgS and polymeric organic species. The strong Mg^{2+}–DME interaction also induces slow desolvation of Mg^{2+}. (b) With the presence of the TEP additive in $Mg(TFSI)_2$/DME electrolyte, the CIPs are significantly interrupted with consequently much less decomposition of the $TFSI^-$ anion. Slow desolvation of the Mg^{2+} solvation sheath is still an issue, nonetheless, leading to large Mg crystal deposits. (c) The adoption of co-ethers changes the solvation structure of Mg^{2+}, leading to a more facile desolvation process that allows the formation of dendrite-free, nanoscale Mg nucleation and growth.

Published on 16 November 2023. Downloaded on 8/23/2025 1:21:11 PM.

activity at the anode and facile anion storage chemistry at the cathode using commercial $Mg(TFSI)_2$ as the salt. A family of methyl phosphates ($(CH_3)_3(CH_2)_nPO_4$, n = 0–4) with high dielectric constants and donor numbers were selected as electrolyte additives to interrupt [Mg^{2+}–$TFSI^-$] CIPs (Scheme 1(b)). This results in suppressed $TFSI^-$ reduction, which limits the thickness of the passivation layer and greatly lowers the voltage hysteresis for Mg plating/stripping. To further improve the Mg anode reversibility and stability, different ethers were chosen as co-solvents to tune the Mg^{2+} solvation sheath, thus facilitating desolvation and nanoscale Mg nucleation/growth (Scheme 1(c)). By combining advanced spectroscopy techniques, molecular dynamics (MD) simulations, and density-functional-theory (DFT) calculations, the Mg^{2+} solvation structure and its interaction with anions or solvents are disclosed in depth. The optimized CEPE electrolytes sustain highly reversible Mg plating/stripping behavior at a range of current densities. We demonstrate ultra-stable Mg plating/stripping for over 7000 hours (9.7 months) at a practical current density of 2 mA cm^{-2} and an areal capacity of 2 mA h cm^{-2}. Importantly, the $>$ 4 V anodic stability of these electrolytes enables polyaniline||Mg full cells to perform up to 3.5 V for over 400 cycles at a fast 2C rate with excellent capacity retention.

Results and discussion

Highly reversible and stable Mg plating/stripping in CEPE

We considered three electrolytes to evaluate their Mg plating/stripping behavior (see Methods and Table S1, ESI†): (1) 0.4 M $Mg(TFSI)_2$/DME as the baseline electrolyte; (2) 0.4 M $Mg(TFSI)_2$/DME : triethyl phosphate (TEP) [10 : 1 in vol, denoted as $Mg(TFSI)_2$/DME:TEP]; and (3) tailor-designed $Mg(TFSI)_2$/CEPE [0.4 M $Mg(TFSI)_2$/DME : diethylene glycol dimethyl ether (G2) : bis(2,2,2-trifluoroethyl) ether (BTFE) : TEP, 19 : 19 : 2 : 4 in vol]. The molar ratio of Mg^{2+} : TEP in the latter two electrolytes is ~1 : 1. Instead of alkoxyborate/aluminate or carborane-based Mg salts, commercially available $Mg(TFSI)_2$ was chosen as the salt, both on the basis of cost and owing to its strong ion pairing in ether-type electrolytes which we sought to disrupt with electrolyte design. TEP was chosen as a stronger donor (coordinating) solvent than glyme, while BTFE is a non-coordinating solvent. These choices of salt and solvents give us a good platform to understand the effect of cation/anion-solvent interaction on interfacial charge transfer in Mg plating/stripping. The optimal solvent ratios were determined through multiple experiment trials (Fig. S1, ESI†). Fig. 1(a) and (b) shows the voltage profiles of these electrolytes in Mg||Mg symmetric cells at a current density of 0.1 mA cm^{-2}. In $Mg(TFSI)_2$/CEPE, a very low Mg plating/stripping overpotential of ~0.15 V was obtained – nearly two-fold lower than in $Mg(TFSI)_2$/DME:TEP (~0.3 V) – whereas in $Mg(TFSI)_2$/DME more than a magnitude higher overpotential of ~1.85 V was observed. The superiority of $Mg(TFSI)_2$/CEPE was further confirmed by the fast-kinetics of Mg plating/stripping at different current densities (Fig. 1(c) and Fig. S2, ESI†), which reveals a low Mg plating/stripping overpotential of $<$0.5 V even at 10 mA cm^{-2}. In contrast, the cell with $Mg(TFSI)_2$/DME:TEP quickly shorted at 1 m A cm^{-2} (Fig. 1(c) and Fig. S1, ESI†) and $Mg(TFSI)_2$/DME shows a continuously high overpotential up to ~3.5 V (Fig. S3, ESI†).

While we observe improved Mg reversibility with TEP, the stability of the Mg anode during long-term cycling is of even greater importance.[12,32,34,35] We investigated Mg||Mg symmetric cell behaviour in different electrolytes. At a practical current density of 2 mA cm^{-2} and areal capacity of 2 mA h cm^{-2} (Fig. 1(d)), cells with $Mg(TFSI)_2$/DME and $Mg(TFSI)_2$/DME:TEP undergo rapid short circuiting after only 2 and 12 hours, respectively. In contrast, cells employing $Mg(TFSI)_2$/CEPE undergo robust stripping/plating for over 7000 hours (9.7 months) without significant increase in voltage hysteresis, and exhibit a total cumulative capacity of over 14 A h cm^{-2}. The overpotential of Mg plating/stripping stabilizes at around 500 mV with no sudden voltage drops, ruling out the possibility of (soft) short circuits, as also confirmed by a charge transfer resistance of about 400 Ω attained after 7000 hours (Fig. S4, ESI†). To the best of our knowledge, this represents unprecedented stability and performance of Mg plating/stripping under such demanding conditions (Table S2, ESI†), suggesting good promise for long-life practical RMBs. The coulombic efficiency (CE) of Mg plating/stripping was investigated using Mg||Au asymmetric cells by a modified Aurbach method reported by Zhang *et al.*[20,36] The highest CE of 95.2% was achieved in $Mg(TFSI)_2$/CEPE (Fig. 1(e)), which is significantly greater that of $Mg(TFSI)_2$/DME:TEP (70.9%). Therefore, the cumulative irreversible capacity over 7000 hours of plating/stripping (3500 cycles, Fig. 3(d)) in the CEPE electrolyte is only 2.4% of its total cumulative capacity. The baseline $Mg(TFSI)_2$/DME electrolyte, in contrast, shows very limited Mg plating/stripping reversibility with only 6.1% CE due to pronounced electrolyte decomposition. While the increase in CE from DME/TEP to CEPE is remarkable, the latter's CE is not quite as high as achieved in bulky-anion salt alkoxyborate/aluminate[16–18] or carborane-based electrolytes.[15,20] This is probably due to the persistence of a low fraction of [Mg^{2+}–$TFSI^-$] contact-ion pairs (despite the major disruption of their formation, see discussion below), which are more easily reduced on the Mg surface.[28]

The charge transfer process at the Mg/electrolyte interface was further explored by electrochemical impedance spectroscopy (EIS) studies (Fig. 1(f)). In $Mg(TFSI)_2$/CEPE, a very low charge transfer resistance (R_{CT}) was observed in a Mg||Mg symmetric cell, consistent with its superior rate performance. On the other hand, $Mg(TFSI)_2$/DME:TEP, despite exhibiting the highest ionic conductivity of 6.4 mS cm^{-1} among the three electrolytes (Fig. S5, ESI†), shows significantly higher R_{CT} than $Mg(TFSI)_2$/CEPE. This suggests interfacial electrochemistry plays a dominant role during Mg plating/stripping. Indeed, diffusion-limited tails ascribed to ion diffusion *via* as-formed interfacial Mg^{2+}-conducting SEIs[37] were observed in the low-frequency region in both electrolytes. In $Mg(TFSI)_2$/DME, however, the very large charge transfer resistance is similar to that of many previous reports (Fig. S6, ESI†).[15,27,34] This is due to electrolyte decomposition on the Mg surface that forms an

 This journal is © The Royal Society of Chemistry 2024

Published on 16 November 2023. Downloaded on 8/23/2025 1:21:11 PM.

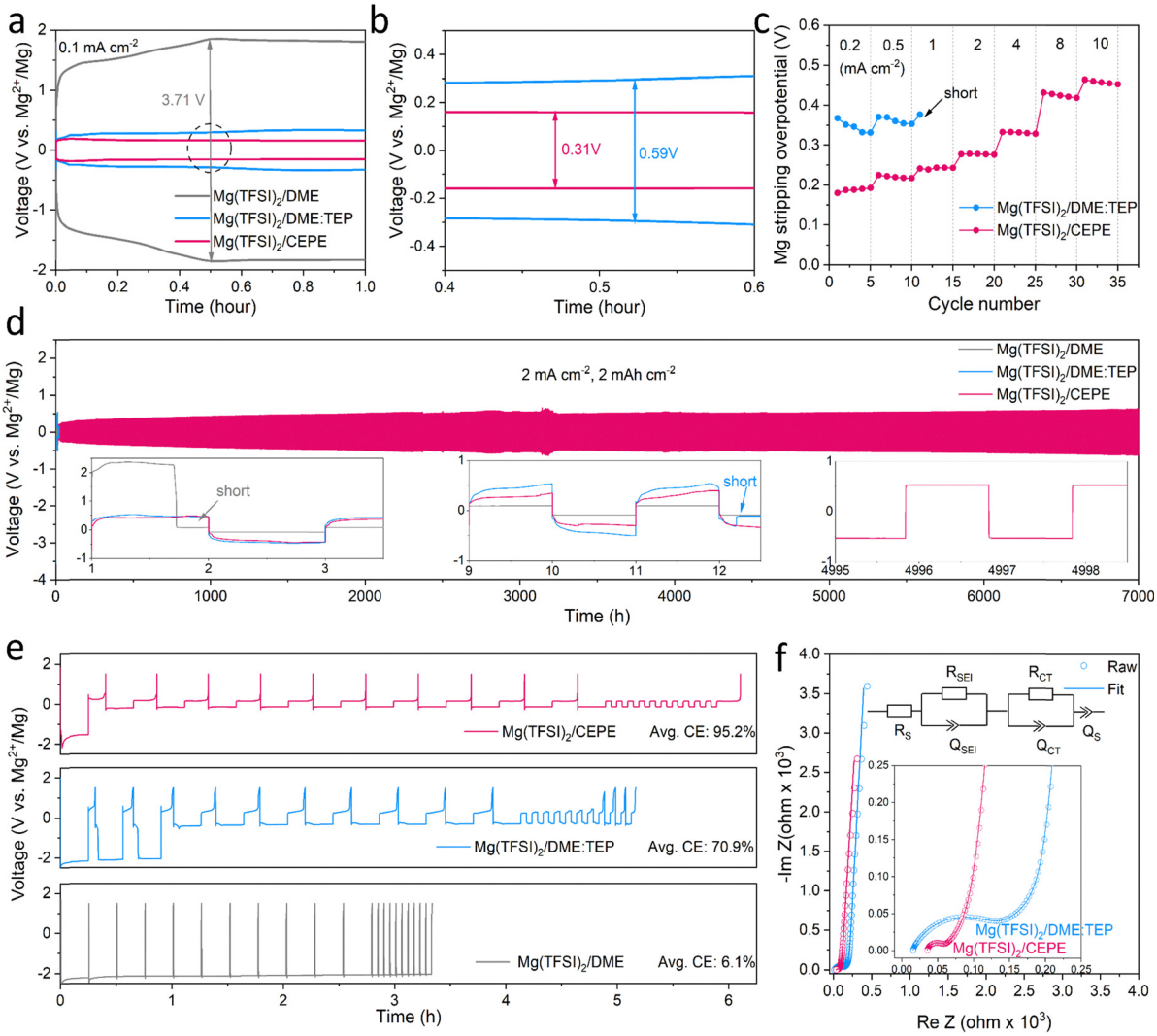


Fig. 1 (a) The 10th voltage profiles of Mg||Mg symmetric cells with different electrolytes at a current density of 0.1 mA cm^{-2} for 1.0 h, with (b) the magnified views of circled regions. (c) Rate performance of Mg||Mg symmetric cells. The areal capacity was fixed at 0.1 mA h cm^{-2}, and the stripping overpotential at the central point was collected. (d) Long-term stability of Mg plating/stripping in different electrolytes at 2 mA cm^{-2} (2 mA h cm^{-2}). The rectangular profile with an overpotential of 0.5 V in the symmetric cell at ultra-long cycling times is characteristic of a low energy for nucleation of Mg on magnesium that is not fully stripped on the previous cycle. (e) Voltage profiles of Mg||Au asymmetric cells with different electrolytes at 0.5 mA cm^{-2}. (f) Nyquist plots of the Mg||Mg symmetric cell after 10 cycles in TEP-based electrolytes. The data were fit (solid line) with the indicated equivalent circuit.

interfacial (Mg^{2+}-insulating) passivation layer, which leads to the absence of a diffusion-limited tail.

Minimized anion activity by phosphates

The role of TEP in CEPE was systematically explored by controlling the DME : TEP ratio, which is directly correlated to Mg^{2+}/Mg redox activity. Fig. 2(a) shows the Mg plating curves of the initial five cycles of Mg||Mg symmetric cells with different DME : TEP ratios. The Mg plating overpotential shows a TEP concentration-dependent behavior, identifying a DME : TEP ratio of 50 : 3 as an effective "sweet" spot to unlock fast Mg plating/stripping, and corresponding to a Mg^{2+} : TEP molar ratio of 10 : 7. This is directly correlated to the CIP fraction in the electrolytes, as revealed by fitting Raman spectra of the $TFSI^-$ band in the 700–770 cm^{-1} region based on a well-established theory of SSIPs and CIPs (Fig. 2(b)).[9,32,38] An abrupt decrease in CIP fraction from 40% to <30% is observed in DME : TEP (50 : 3), matching the sharp drop in plating overpotential to −0.32 V (Fig. 2(c)). It indicates a threshold in CIP fraction where facile Mg^{2+}/Mg redox activity is unlocked below that limit, and Mg^{2+} desolvation from coordinated solvents at the interface starts to play a critical role (see below). Indeed, previous studies report that significant reduction of CIPs at the Mg surface suppresses $TFSI^-$ activity.[28,29] This is verified by the remarkable decrease of F/S signals from decomposed $TFSI^-$ in the energy-dispersive X-ray spectra (EDX, Fig. 2(d)) of $Mg(TFSI)_2$/DME:TEP, in contrast to the strong F/S signals in $Mg(TFSI)_2$/DME (Fig. 2(e)).

To reveal the functionality of TEP in suppressing anion reduction activity, density-functional-theory (DFT) calculations

Published on 16 November 2023. Downloaded on 8/23/2025 1:21:11 PM.

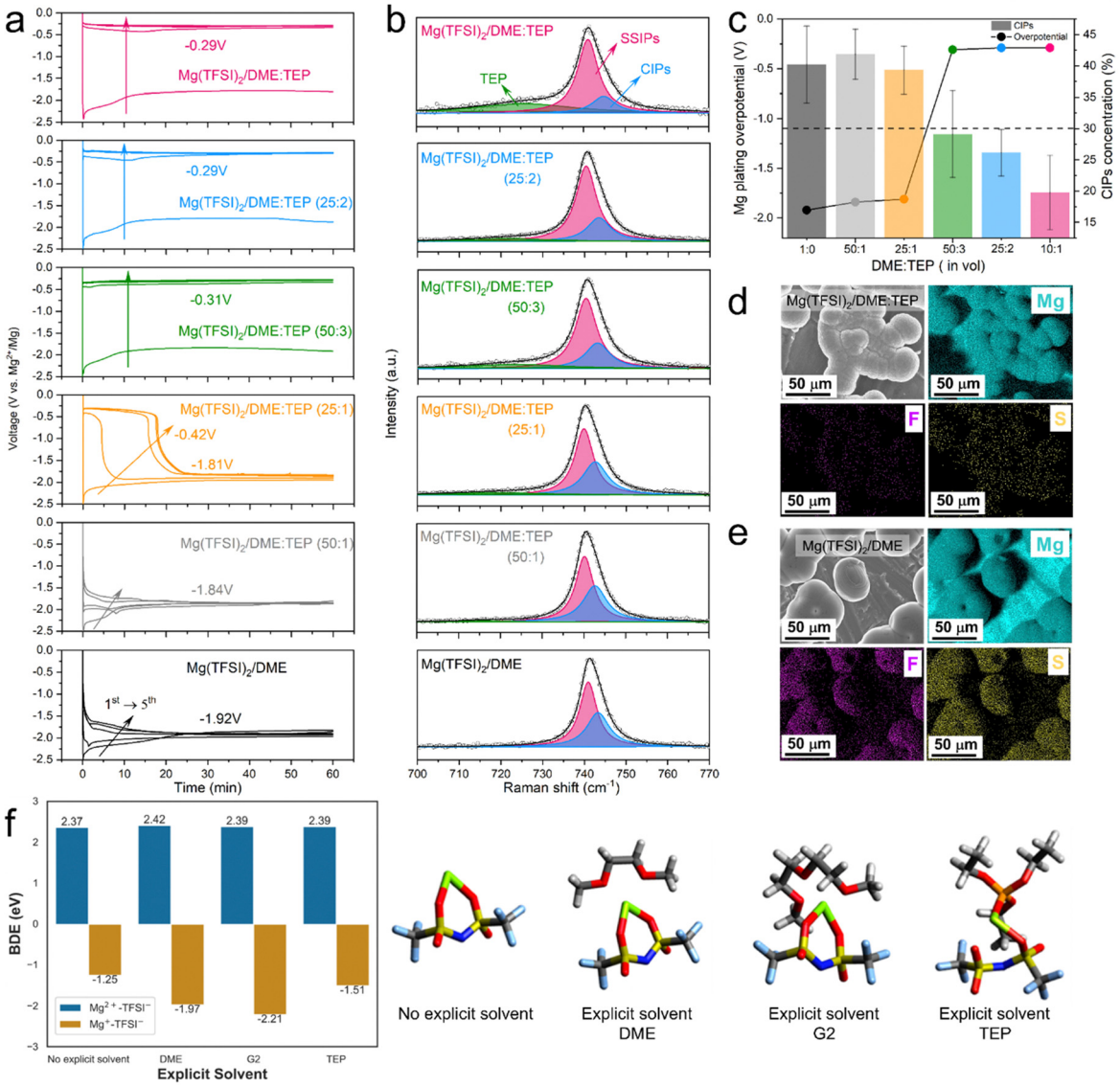


Fig. 2 (a) The initial five plating profiles of $Mg(TFSI)_2$/DME in Mg||Mg symmetric cells with different DME : TEP ratios at a current density of 0.1 mA cm^{-2} (b) corresponding Raman spectra of different electrolytes in the 700–770 cm^{-1} range (the overall fit (black) has three components: TEP-green, SSIPs-pink and CIPs-blue). All fits were based on a Lorentzian peak function with coefficient of determination $R^2 > 0.997$. (c) The Mg plating overpotential and the ratio of CIP content as a function of DME : TEP ratio. (d) and (e) SEM images and EDX mapping of plated Mg in (d) $Mg(TFSI)_2$/DME:TEP and (e) $Mg(TFSI)_2$/DME. (f) DFT calculations of C–S bond dissociation energies of [Mg^{2+}–$TFSI^-$] and transient [Mg^+–$TFSI^-$] CIPs in different coordinating environments with the explicit solvent coordinated structure shown on the right.

were performed. In an implicit solvent, thermodynamically endergonic C–S bond dissociation was observed in the [Mg^{2+}–$TFSI^-$] CIPs (bond dissociation energy (BDE): 2.37 eV, Fig. 2(f)), whereas partially reduced transient [Mg^+–$TFSI^-$] CIPs show exergonic C–S bond dissociation (BDE: −1.25 eV), consistent with previous studies.[28] The C–S bond dissociation accompanies complete reduction of Mg^+ to Mg^0 (Fig. S7, ESI†) and essentially enables an irreversible plating process. More exergonic C–S bond cleavage was obtained for [Mg^+–$TFSI^-$] CIPs surrounded by one explicit DME (BDE: −1.97 eV) or G2 molecule (BDE: −2.21 eV), emphasizing the co-solvation during charge transfer does not protect the $TFSI^-$ anions from reduction. The BDE is also exergonic (−1.51 eV) for a transient CIP surrounded by an explicit TEP molecule. In the molecular dynamics (MD) results (see Fig. 3(b) below), the paired Mg fraction decreases by ∼50% in the CEPE system when compared to the $Mg(TFSI)_2$:DME system. These results, in conjunction with the Raman spectra (Fig. 2(b)), confirm that the introduction of TEP successfully outcompetes the $TFSI^-$ anions in the first solvation shell and significantly reduces the CIP concentration. Nonetheless, it is not reduced to zero. While the residual CIPs in CEPE could still induce limited anion decomposition, this may be further inhibited by applying interfacial protective coatings on the Mg surface,[39] or by additional electrolyte design that is beyond the scope of this work.

Similar effects on activating reversible Mg^{2+}/Mg redox in single DME solvents extends to other phosphates with a formula of

 This journal is © The Royal Society of Chemistry 2024

Published on 16 November 2023. Downloaded on 8/23/2025 1:21:11 PM.

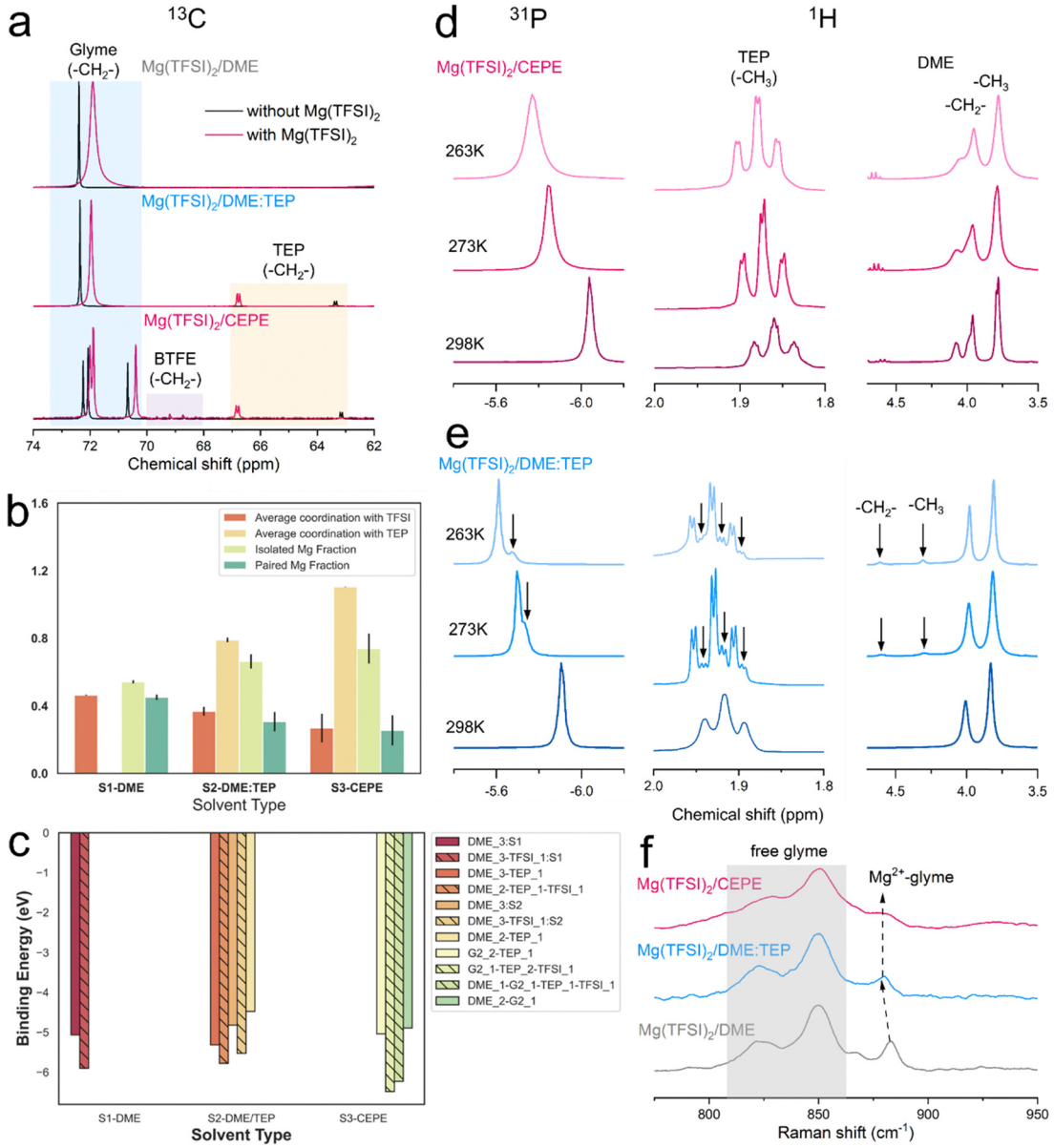


Fig. 3 (a) ^{13}C NMR spectra of different electrolytes with/out $Mg(TFSI)_2$ at 298 K. (b) MD simulations of Mg^{2+} coordination environments in different electrolytes. The *y*-axis indicates either the average coordination numbers or the fraction of Mg^{2+} clusters (c) DFT calculations of binding energies of predominant Mg^{2+} solvation shells. (d) and (e) Variable temperature ^{31}P and ^{1}H NMR spectra in (d) $Mg(TFSI)_2$/CEPE and (e) $Mg(TFSI)_2$/DME:TEP. Smaller peaks observed at lower temperature are indicated by black arrows. (f) Raman spectra of various electrolytes in the region between 775–950 cm^{-1}.

$(CH_3)_3(CH_2)_nPO_4$ (n = 0–4, Fig. S8, ESI†). The co-ether engineering approach functions similarly (for example, TMP with n = 0), albeit with poorer rate characteristics relative to TEP (Fig. S9 and S10, ESI†). Nonetheless, these phosphates with different numbers of methylene groups can behave very differently. Previous reports indicate TMP primarily displaces one DME from the Mg^{2+} solvation structure to suppress DME reduction by forming TMP-reduced SEIs,[34,35] but significant $TFSI^-$ decomposition still occurs during Mg plating/stripping. The greater steric effect created by methylene groups in TEP may play a pivotal role in controlling interfacial activity of both the $TFSI^-$ anion and these phosphates. This directly relates to the electrochemical stability of the electrolytes (see the discussion below).[40] More importantly, adding these phosphates to a single ether solvent (DME) delivers poor Mg anode stability even at a low current density of 0.1 mA cm^{-2} and areal capacity of 0.1 mA h cm^{-2} (Fig. S8, ESI†), which is inadequate for practically fast-charging Mg batteries. The optimized CEPE in this study represents a universal strategy to achieve benchmark-level Mg plating/stripping performance that applies to different phosphates (Fig. S10, ESI†). We further reveal the critical role of co-ethers in $Mg(TFSI)_2$/CEPE to modify the Mg^{2+} solvation structure and plating/stripping morphology below.

Optimized solvation structures of Mg^{2+}

We carried out nuclear magnetic resonance (NMR) spectroscopy to understand the solvation structure of the electrolytes

Published on 16 November 2023. Downloaded on 8/23/2025 1:21:11 PM.

in these CEPE systems. Fig. 3(a) displays the ^{13}C NMR spectra of various electrolytes at 298 K. In both $Mg(TFSI)_2$/CEPE and $Mg(TFSI)_2$/DME:TEP, the Mg^{2+}–TEP interaction leads to high frequency shifts of the $-CH_2-$ groups in TEP by ~3.7 and ~3.4 ppm, respectively. This interaction is much stronger than that of Mg^{2+}–DME in $Mg(TFSI)_2$/DME, which only provokes a 0.5 ppm low frequency shift of the DME $-CH_2-$ group. This strong Mg^{2+}–TEP interaction results in a large decrease of the full width at half maximum (FWHM) of DME (the $-CH_2-$ signal) by around 60% (Table S3, ESI†): a clear indication of a much lesser CIP fraction.[28] This is in perfect accord with Raman analysis (Fig. S11, ESI†). A similar Mg^{2+}–TEP interaction was observed in both $Mg(TFSI)_2$/CEPE and $Mg(TFSI)_2$/DME:TEP electrolytes (Fig. S12, ESI†), suggesting the consistent effect of reducing CIPs in all electrolytes with the presence of TEP.

The reduction in CIP formation by TEP is further upheld by classical MD simulations (Fig. 3(b)). Mg^{2+} shows strong interaction with the oxygen of the P=O motif of TEP (Fig. S13, ESI†). The average Mg^{2+}–TEP coordination increases from ~0.8 in $Mg(TFSI)_2$/DME:TEP to ~1.1 in $Mg(TFSI)_2$/CEPE. The fractions of isolated and paired Mg^{2+} ions – defined by solvation shells with zero and one $TFSI^-$ anion – were also calculated. The paired Mg^{2+} fractions from MD closely matches with the experimental CIP concentrations (Fig. S9, ESI†), which is especially impressive with a non-polarizable forcefield:[41] the average paired Mg^{2+} fraction decreases from ~0.45 in $Mg(TFSI)_2$/DME (experimental CIP concentration: ~40%) to ~0.26 in $Mg(TFSI)_2$/CEPE (experimental CIP concentration: ~23%). Fig. S14 (ESI†) shows the increasing diversity of the solvation shell population distributions in $Mg(TFSI)_2$/CEPE compared to that in $Mg(TFSI)_2$/DME, which suggests that a higher electrolyte entropy enables complete salt [$Mg(TFSI)_2$] dissociation and allows Mg^{2+} ions to form fully solvated clusters.[42] Moreover, the average coordination between Mg^{2+} and $TFSI^-$ steadily falls with a concomitant rise in isolated Mg^{2+} and free $TFSI^-$ species (Fig. S15, ESI†). This is a consequence of the simultaneous competition between DME, TEP and G2 (in $Mg(TFSI)_2$/CEPE) to displace the $TFSI^-$ anion from the Mg^{2+} solvation environment in the phosphate-added systems (Fig. S16, ESI†). The G2 molecules – with three polar O atoms – can maximally participate in tridentate coordination with Mg^{2+} ions, while DME is only capable of monodentate or bidentate coordination. Consequently, the average coordination between Mg and DME is significantly lower in the CEPE system (Fig. S16, ESI†). A sharp Mg–O radial distribution function (RDF) peak at ~2.1 Å and the displaced position of the Mg–N RDF peak at ~4 Å (Fig. S11, ESI†) confirms that the O from the sulfonyl group dominates the interaction between Mg^{2+} and $TFSI^-$ in the first solvation shell.[43] The negligible coordination between Mg and BTFE (Fig. S17, ESI†) is consistent with previous studies.[30,44] These results provide strong support to the experimental results and confirm the decrease of CIPs in both the $Mg(TFSI)_2$/DME:TEP and $Mg(TFSI)_2$/CEPE electrolytes.

DFT calculations were further performed to calculate the binding energies of the predominant clusters in these electrolytes (Fig. S14, ESI†). The results in Fig. 3(c) demonstrate that the clusters with CIPs in the solvation shells (hatched bars) consistently exhibit a greater binding energy than fully solvent-coordinated Mg^{2+}, in turn suggesting a higher desolvation energy for the charge transfer process.[45,46] The direct correlation between binding and desolvation energy is already established.[47] The trends in Fig. 3(c) indicate that the large decrease in CIPs and increase in exclusively solvent-coordinated Mg^{2+} solvated clusters promote a facile desolvation process during charge transfer.[48] The results also affirm that the observed fast kinetics of Mg plating/stripping in the CEPE system is induced by higher exchange current densities and surface energies which in turn promotes uniform Mg electrodeposition (see below).[45]

The bulk dynamics of ethers and TEP in these electrolytes were explored by conducting variable temperature NMR. In both ^{31}P and ^{1}H spectra of $Mg(TFSI)_2$/CEPE, no new peaks were found at low temperature (Fig. 3(d)). In $Mg(TFSI)_2$/DME:TEP, however, the single ^{31}P resonance at 298 K was gradually split into two at below 273 K (Fig. 3(e)), along with the appearance of more $-CH_3$ and $-CH_2-$ signals of TEP in ^{1}H spectra at low temperature (Fig. S18, ESI†). This peak splitting suggests Mg^{2+} is undercoordinated with TEP (*e.g.* fewer Mg^{2+}–TEP bonds in the presumably six-coordinated Mg^{2+} solvation sheath). In addition, the Mg^{2+}–DME interaction in $Mg(TFSI)_2$/DME:TEP shows similar undercoordination with two new higher-frequency peaks appearing in ^{1}H spectra below 273 K. These were assigned to the $-CH_2-$ and $-CH_3$ groups of DME by carrying out a Heteronuclear Single Quantum Coherence (HSQC) experiment (Fig. S19, ESI†). The new peaks can be ascribed to the slow exchange rate of DME molecules in different bound environments,[30,49] leading to peak separation at low temperatures. The addition of G2 and BTFE in $Mg(TFSI)_2$/CEPE effectively enhances the exchange rate, owing to the absence of such undercoordination behavior. This is because G2 is known to exchange much faster than DME while BTFE barely coordinates with Mg^{2+},[30] in turn indicating decreased Mg^{2+}–glyme interaction by co-ethers. This is verified by the blue shift and decreased intensity of coordinated glyme signals in the Raman spectra (Fig. 3(f)),[12,34] As a consequence, a lower desolvation penalty can be expected in $Mg(TFSI)_2$/CEPE, which explains the much enhanced kinetics of Mg plating/stripping relative to $Mg(TFSI)_2$/DME:TEP (Fig. 1).

Tuning nanoscale and dendrite-free Mg plating/stripping morphology

To delve more into the function of co-ethers in sustained long-term Mg plating/stripping, we used scanning electron microscopy (SEM) coupled with EDX to probe the Mg electrodes retrieved from Mg||Mg symmetric cells. In $Mg(TFSI)_2$/CEPE, nanoscale Mg nuclei of around 10 nm were observed with much smoother surface morphology that merged into globules (Fig. 4(a), (c) and Fig. S20, ESI†). The X-ray diffraction (XRD) pattern of plated Mg confirms that these deposited globules are agglomerated fine particles (Fig. S21, ESI†). In $Mg(TFSI)_2$/DME:TEP, however, Mg deposits as microscale flaky crystals with a dimension of ~500 nm (Fig. 4(b) and (d)). Mg plated in

 This journal is © The Royal Society of Chemistry 2024

Published on 16 November 2023. Downloaded on 8/23/2025 1:21:11 PM.

$Mg(TFSI)_2$/DME yielded a spherical morphology of core–shell multilayers (Fig. 2(e) and Fig. S22, ESI†). The nanoscale nucleation and growth in $Mg(TFSI)_2$/CEPE leads to denser and thinner hemisphere deposition with a thickness of ~20 μm, in contrast to ~60 μm in $Mg(TFSI)_2$/DME:TEP. The uniform deposition in CEPE can be attributed to the increase in isolated Mg^{2+} clusters with lower binding energies and weakened Mg^{2+}–DME interactions (Fig. 3) that results in a faster desolvation process at the Mg/electrolyte interface. We thus expected a more homogeneous distribution of local interfacial currents during stripping (Fig. 4(e) and (f)), which was verified by the smoother and cleaner stripping morphologies in $Mg(TFSI)_2$/CEPE (Fig. 4(g)). In $Mg(TFSI)_2$/DME:TEP, by comparison, large quantities of cracked Mg globules were observed on the cycled electrode (Fig. 4(h)). We believe that voids can be formed between the flaky crystals due to a non-uniform distribution of stripping current (Fig. S23, ESI†), which leads to electrolyte penetration through the plated Mg globules and results in inactive Mg.[50] With continuous plating/stripping, the accumulation of cracked globules leads to a mossy surface that can easily induce short circuits (Fig. S24, ESI†). Therefore, Mg||Mg symmetric cells show outstanding stability with $Mg(TFSI)_2$/CEPE but quickly short with $Mg(TFSI)_2$/DME:TEP. In $Mg(TFSI)_2$/DME, the thick insulating passivation layer resulting from electrolyte decomposition significantly blocks the electron transfer pathway and thus Mg dissolution during the stripping process, preserving the original spherical morphology (Fig. S25, ESI†).

Interfacial SEI chemistry on the plated Mg surface

High-resolution X-ray photoelectron spectroscopy (XPS) was used to investigate SEI compositions on the plated Mg surface in different electrolytes. For Mg cycled in the baseline $Mg(TFSI)_2$/DME (Fig. 5(a)), we observed abundant surface species including MgF_2 (688.5 eV, F 1s), MgS (163.2 eV, S 2p), –CF (686.2 eV, F 1s) and $-SO_x$ ($x < 2$, 167.4 eV, S 2p). These likely result from the reduction of $TFSI^-$ anions. In addition, F-rich $-CF_3$ (688.6 eV, F 1s) and $-SO_2$ (169.2 eV, S 2p) signals imply copious adsorption of $TFSI^-$ anions on the Mg surface (Fig. 5(b)). These results correlate with the large fraction of CIPs in the electrolyte, which facilitates the adsorption and reduction of $TFSI^-$ on the Mg surface to form the passivation layer. Owing to the significantly decreased CIPs in $Mg(TFSI)_2$/DME:TEP, intensities in the F 1s and S 2p region are greatly diminished on plating Mg, showing effective suppression of these anion-related species. In $Mg(TFSI)_2$/CEPE, no evident of anion-derived species were observed. We attribute this to the G2-optimized solvation structure and the adsorption of BTFE on the Mg surface that further suppresses the decomposition of $TFSI^-$ (Fig. 5(c)). Indeed, the $Mg(TFSI)_2$/CEPE without trace BTFE shows more electrolyte decomposition products (Fig. S26, ESI†), with significantly poorer kinetics of Mg plating/stripping (Fig. S27, ESI†). In addition, no phosphorus signals were found for electrodes retrieved from both $Mg(TFSI)_2$/DME:TEP and $Mg(TFSI)_2$/CEPE (Fig. S28, ESI†), suggesting TEP is not decomposed. This is in strong contrast to previous studies on the TMP additive that showed its extensive reduction to form a $Mg_3(PO_4)_2$-rich interface,[34,35] which implies additive consumption causes the continuous increase of voltage hysteresis during Mg plating/stripping. While it is surprising that the additional $-CH_2$ group in TEP results in remarkably increased stability against electrochemical reduction, we speculate that this originates from a steric effect. This results in different Mg^{2+} solvation structures that presumably exist with higher stability.[40] Identifying the exact origin of this difference is beyond the scope of this work and will be part of a future study.

The structural characteristics and chemical mapping of these interfaces formed on Mg were further probed using cryogenic focused ion beam (Cryo-FIB) milling and transmission electron microscopy (TEM). Fig. 6(a) and (b) shows the high-angle annular dark-field (HAADF) images at the surface of Mg deposited in $Mg(TFSI)_2$/CEPE and $Mg(TFSI)_2$/DME:TEP, along with maps showing the Mg/S and Mg/F elemental

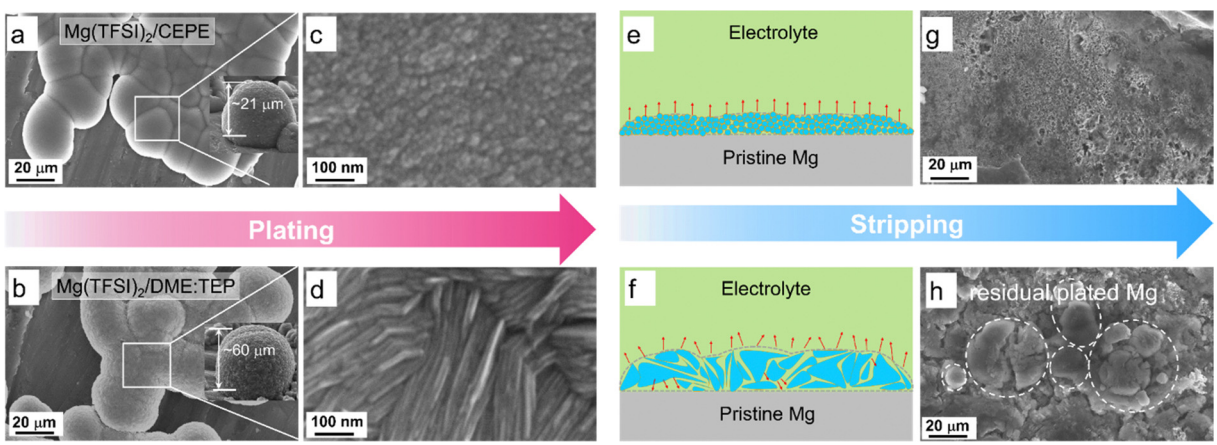


Fig. 4 (a)–(d) Plated Mg morphologies (insets are the images of representative Mg globules with estimated thickness from a tilt angle of 60°). (e) and (f) Schematic illustration of stripping current distribution on plated Mg. (g) and (h) Fully stripped Mg morphologies in different electrolytes: (a), (c), (e) and (g) $Mg(TFSI)_2$/CEPE; (b), (d), (f) and (h) $Mg(TFSI)_2$/DME:TEP. All electrodes were retrieved from Mg||Mg symmetric cells that were cycled at a current density of 1 mA cm^{-2} and areal capacity of 1 mA h cm^{-2}.

Published on 16 November 2023. Downloaded on 8/23/2025 1:21:11 PM.

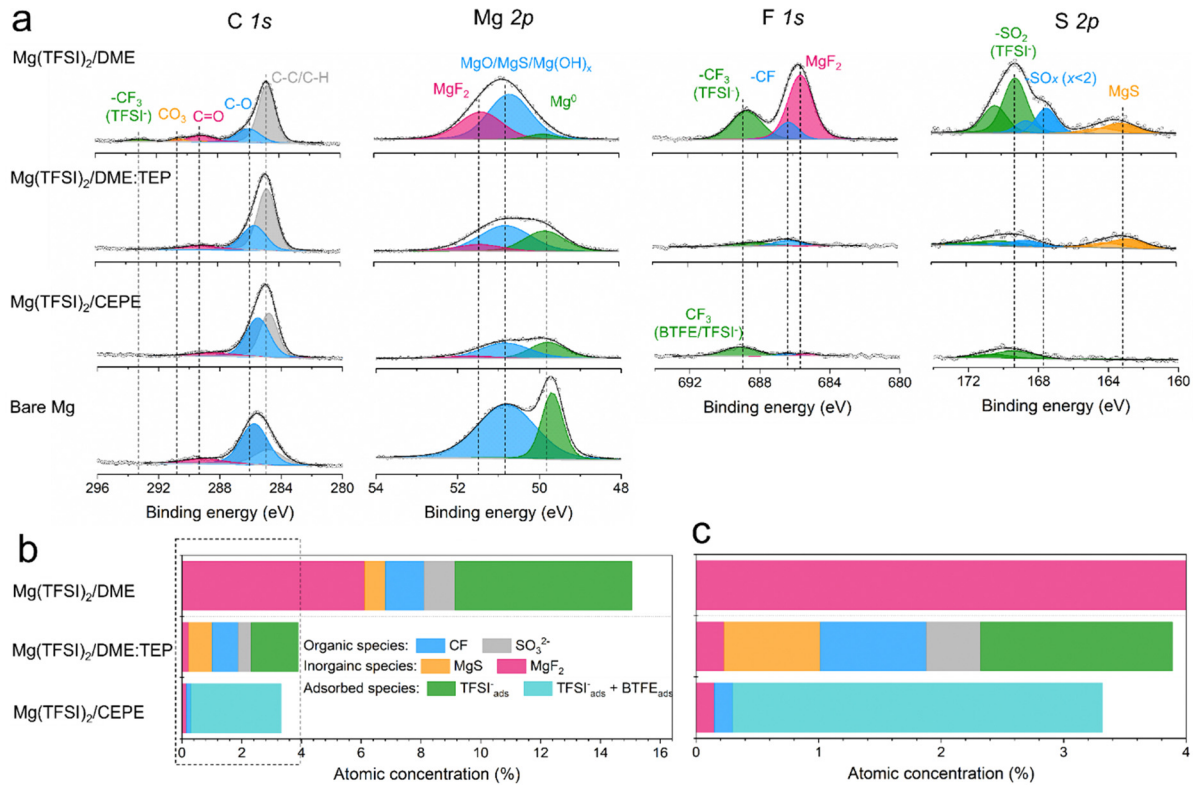


Fig. 5 (a) XPS spectra of bare Mg and plated Mg in different electrolytes. (b) and (c) Atomic concentration of different $TFSI^-$-related species on the plated Mg surface and (c) magnified view of the circled region.

distribution. Trace amounts of S and F can be observed on the Mg surface that originate from the formation of a very thin SEI. This is in good accord with the XPS results above. The thickness cannot be well defined due to the low quantity of S/F present that is comparable to the background noise. In contrast, in baseline $Mg(TFSI)_2$/DME (Fig. 6(c)), a ~30 nm thick S-rich and F-rich passivation layer is formed. In addition to the accumulation of S/F at the interface, significant amounts decorate the

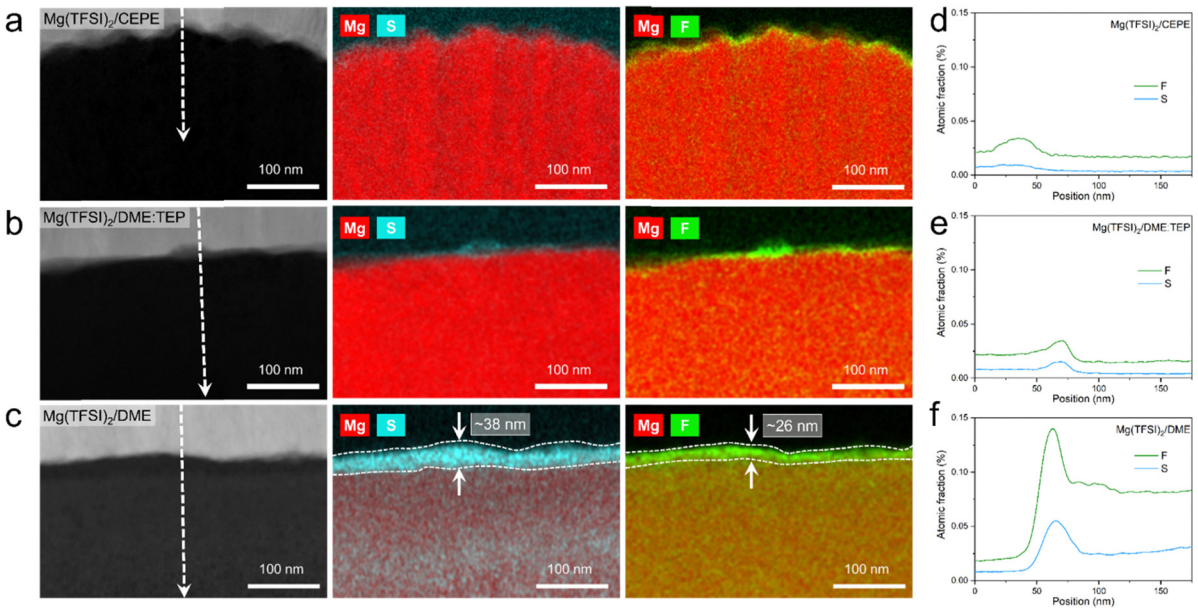


Fig. 6 (a)–(c) STEM-HAADF images with Cr coating (white) on top of Mg samples (black) and corresponding EDX chemical maps with Mg/S and Mg/F overlap. (d)–(f) distribution of F and S by EDX line scan analysis taken along the indicated lines shown in STEM-HADDF images. (a) and (d) Mg(TFSI)2/CEPE; (b) and (e) Mg(TFSI)2/DME:TEP; (c) and (f) $Mg(TFSI)_2$/DME.

 This journal is © The Royal Society of Chemistry 2024

Published on 16 November 2023. Downloaded on 8/23/2025 1:21:11 PM.

underlying Mg region. In both $Mg(TFSI)_2$/DME:TEP and $Mg(TFSI)_2$/CEPE, the S/F species were greatly diminished at both surface and Mg regions, as confirmed by EDX line scan analysis (Fig. 6(d)–(f) and Fig. S29, ESI†).

High-voltage stability in Mg-organic cathode full cells

To assess the anodic stability of the CEPEs, linear scan voltammetry (LSV) was performed on three-electrode cell with commercial Al foil as a working/counter electrode and Mg as the reference electrode. A typical scan rate of 5 mV s^{-1} was used in the measurements.[17] All electrolytes exhibit an oxidation stability of around 4 V on Al foil (Fig. 7(a) and Fig. S30, ESI†), consistent with previously reported $Mg(TFSI)_2$/glyme electrolyte systems.[25,33] The low anodic current between 3 V to 4 V (note *y*-scale in the inset) is attributed to the oxidation of trace impurities/moisture in the electrolyte, or minor Al corrosion in the presence of $Mg(TFSI)_2$ as commonly reported.[25] We chose polyaniline (PANI) as a readily available, high-voltage (~2.3 V) organic cathode material to benchmark the oxidative stability of the $Mg(TFSI)_2$/CEPE system. We demonstrate the cycling of a PANI||Mg cell up to a high cut-off voltage of 3.5 V (Fig. 7(b)), providing a specific discharge capacity of 250 mA h g_{PANI}^{-1} at C/10 (1C = 250 mA g_{PANI}^{-1}) with an average discharge voltage of ~2.05 V. The dominant $TFSI^-$ anion storage chemistry is confirmed by EDX analysis (Fig. S31, ESI†), in accord with previous studies.[51] A very large specific capacity of PANI is obtained in part due to CEPE's good oxidative stability, whereas the use of chloride-based electrolytes in previous studies[51] limits PANI's high-voltage application and hence gives rise to a low specific capacity of less than 150 mA h g_{PANI}^{-1} in the range of 0.1–2.8 V. More importantly, PANI in $Mg(TFSI)_2$/CEPE shows excellent rate capability, with a capacity of 239, 215, and 165 mA h g_{PANI}^{-1} at C/2, 1C, and 2C, respectively. In the baseline $Mg(TFSI)_2$/DME electrolyte, however, a high voltage polarization

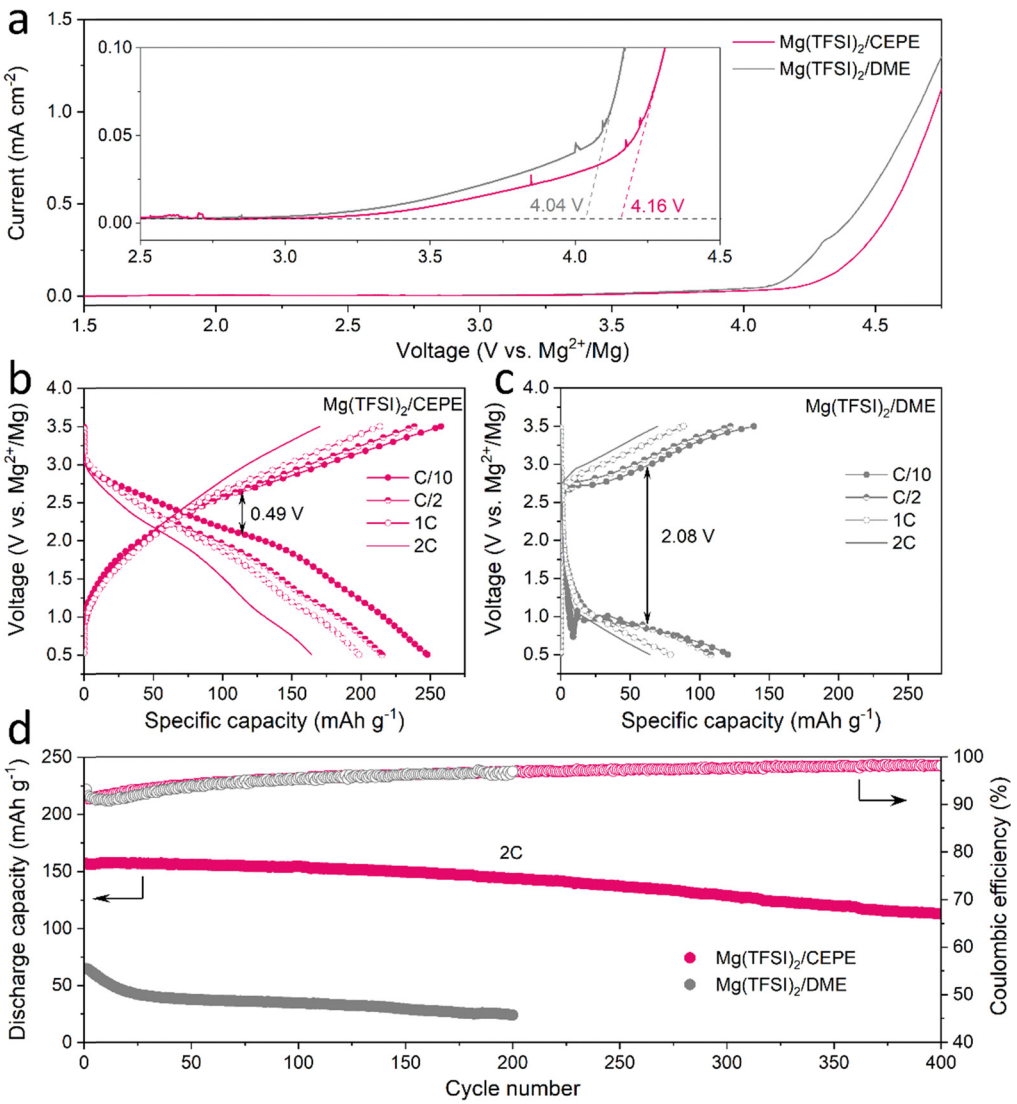


Fig. 7 (a) LSV curves of $Mg(TFSI)_2$/CEPE and $Mg(TFSI)_2$/DME at a scan rate of 5 mV s^{-1}. The onset of oxidation in CEPE is slightly higher at 4.16 V. (b) and (c) Charge–discharge curve of PANI||Mg cells at different rates (1C = 250 mA g_{PANI}^{-1}) in (b) $Mg(TFSI)_2$/CEPE and (c) $Mg(TFSI)_2$/DME. (d) Long-term cycling of PANI||Mg cells at 2C in different electrolytes.

Published on 16 November 2023. Downloaded on 8/23/2025 1:21:11 PM.

of around 2.08 V was observed for the PANI||Mg cell at C/10 (Fig. 7(c)), yielding a discharge capacity of only 120 mA h g^{-1}. The long-term cycling stability of PANI||Mg cell was further investigated at a 2C rate (Fig. 7(d) and Fig. S32, S33, ESI†). In $Mg(TFSI)_2$/CEPE, the cell retains a high discharge capacity of $\sim$ 113 mA h g^{-1} with 99% CE after 400 cycles, corresponding to a capacity retention of over 72%. In contrast, a low discharge capacity of only 65 mA h g^{-1} was obtained in $Mg(TFSI)_2$/DME, which quickly drops to around 24 mA h g^{-1} after 200 cycles due to the poor kinetics of Mg plating/stripping. The desirable performance of PANI in CEPE under high voltage conditions confirms the high oxidative stability of CEPE and suggests a facile anion desolvation process due to suppressed CIP formation. This in turn results in facile desolvation of Mg^{2+} at the cathode side, as proven by using an n-type pyrene-4,5,9,10-tetraone (PTO) cathode that also shows good rate performance (Fig. S34, ESI†). However, the PTO||Mg cell shows limited cycling stability due to the relatively high solubility of Mg_1PTO as reported,[14] and was not pursued further in this study.

Conclusions

A new class of co-ether phosphate electrolytes (CEPE) is developed for stable and high-voltage Mg batteries. This electrolyte system relies on two key components: ethyl phosphate to unlock the activity of Mg^{2+}/Mg redox and co-ether solvents to improve the kinetics and stability of Mg plating/stripping. The complex interactions between cation, anion and solvents were revealed by advanced spectroscopies and MD simulations, providing new design principles for efficient Mg electrolytes. The use of a cost-effective and commercially available Mg salt – $Mg(TFSI)_2$ – simplifies scalability. Importantly, it demonstrates the effectiveness of tuning the solvent to disrupt ion-pair formation, which would not be evident with a bulky-anion salt such as $Mg(CB_{11}H_{12})_2$. Dendrite-free Mg plating/stripping with $Mg(TFSI)_2$ is thus achieved for over 7000 hours ($\sim$10 months) at a practical areal capacity of 2 mA h cm^{-2}. PANI||Mg batteries assembled with the optimized electrolyte provide a capacity of 240 mA h $g_{PANI}{}^{-1}$ at a C/2 rate, and perform over 400 cycles up to an operating voltage of 3.5 V at a 2C rate. These showcase the 4.15 V anodic stability of the $MgTFSI_2$-CEPE system and suggest facile anion desolvation due to suppressed contact-ion pair formation. Furthermore, ready desolvation of the Mg^{2+} cation is demonstrated by good rate performance of a state-of-the-art n-type pyrene-4,5,9,10-tetraone (PTO) cathode. Our weakly ion pairing approach effected by solvent design opens up new frontiers for low-cost and high-voltage electrolyte development that could take advantage of facile desolvation processes at the interfaces, establishing a platform for new avenues of investigation for next generation energy storage in RMBs.

Author contributions

C. L. and L. F. N. designed this study. C. L. prepared the electrolytes, carried out the characterization and all the electrochemical measurements. R. D. G. and K. A. P. performed molecular dynamics and DFT calculation. A. S. performed NMR measurements. C. L. and L. F. N. wrote the manuscript with contributions from the other authors.

Conflicts of interest

The authors declare no competing interests.

Acknowledgements

This work was financially supported by the Joint Centre for Energy Storage Research, an Energy Innovation Hub funded by the US. Department of Energy, Office of Science, Basic Energy Sciences. We would like to thank Dr P. Broderson (University of Toronto) for carrying out the XPS data collection, Dr Ryan Kingsbury, and Dr Jingyang Wang for guidance with the MD calculations, Evan Spotte-Smith for insights on the CIP decomposition and Alexander Epstein for helpful discussions regarding the DFT calculations. L.F.N also acknowledges NSERC for platform support through the Discovery Grant and Canada Research Chair programs.

References

1 R. Mohtadi, O. Tutusaus, T. S. Arthur, Z. Zhao-Karger and M. Fichtner, *Joule*, 2021, **5**, 581–617.
2 Y. Tian, G. Zeng, A. Rutt, T. Shi, H. Kim, J. Wang, J. Koettgen, Y. Sun, B. Ouyang, T. Chen, Z. Lun, Z. Rong, K. Persson and G. Ceder, *Chem. Rev.*, 2021, **121**(3), 1623–1669.
3 M. Kar, O. Tutusaus, D. R. MacFarlane and R. Mohtadi, *Energy Environ. Sci.*, 2019, **12**, 566–571.
4 Y. S. Meng, V. Srinivasan and K. Xu, *Science*, 2022, **378**, 1065.
5 H. Zhang, L. Qiao and M. Armand, *Angew. Chem., Int. Ed.*, 2022, **61**, e202214054.
6 P. Canepa, G. S. Gautam, D. C. Hannah, R. Malik, M. Liu, K. G. Gallaghe, K. A. Persson and G. Ceder, *Chem. Rev.*, 2017, **117**(5), 4287–4341.
7 R. Davidson, A. Verma, D. Santos, F. Hao, C. Fincher, S. Xiang, J. V. Buskirk, K. Xie, M. Pharr and P. P. Mukherje, *ACS Energy Lett.*, 2019, **4**(2), 375–376.
8 M. S. Ding, T. Diemant, R. J. Behm, S. Passerini and G. A. Giffin, *J. Electrochem. Soc.*, 2018, **165**, A1983.
9 Q. Pang, A. Shyamsunder, B. Narayanan, C. Y. Kwok, L. A. Curtiss and L. F. Nazar, *Nat. Energy*, 2018, **3**, 783–791.
10 P. Canepa, S. Bo, G. S. Gautam, B. Key, W. D. Richards, T. Shi, Y. Tian, Y. Wang, J. Li and G. Ceder, *Nat. Commun.*, 2017, **8**, 1759.
11 Y. Liang, H. Dong, D. Aurbach and Y. Yao, *Nat. Energy*, 2020, **5**, 646–656.
12 Y. Sun, Y. Wang, L. Jiang, D. Dong, W. Wang, J. Fan and Y. Lu, *Energy Environ. Sci.*, 2023, **16**, 265–274.
13 D. Aurbach, Z. Lu, A. Schechter, Y. Gofer, H. Gizbar, R. Turgeman, Y. Cohen, M. Moshkovich and E. Levi, *Nature*, 2000, **407**, 724–727.

 This journal is © The Royal Society of Chemistry 2024

Published on 16 November 2023. Downloaded on 8/23/2025 1:21:11 PM.

14 H. Dong, Y. Liang, O. Tutusaus, R. Mohtadi, Y. Zhang, F. Hao and Y. Yao, *Joule*, 2018, **3**, 782–793.
15 O. Tutusaus, R. Mohtadi, T. S. Arthur, F. Mizuno, E. G. Nelson and Y. V. Sevryugina, *Angew. Chem., Int. Ed.*, 2015, **54**, 7900–7904.
16 J. Luo, Y. Bi, L. Zhang, X. Zhang and T. L. Liu, *Angew. Chem., Int. Ed.*, 2019, **58**, 6967–6971.
17 J. T. Herb, C. A. Nist-Lund and C. B. Arnold, *ACS Energy Lett.*, 2016, **1**, 1227–1232.
18 Z. Zhao-Karger, M. E. G. Bardaji, O. Fuhr and M. Fichtner, *J. Mater. Chem. A*, 2017, **5**, 10815–10820.
19 T. Pavčnik, M. Lozinšek, K. Pirnat, A. Vizintin, T. Mandai, D. Aurbach, R. Dominko and J. Bitenc, *ACS Appl. Mater. Interfaces*, 2022, **14**, 26766–26774.
20 H. Dong, O. Tutusaus, Y. Liang, Y. Zhang, Z. Lebens-Higgins, W. Yang, R. Mohtadi and Y. Yao, *Nat. Energy*, 2020, **5**, 1043–1050.
21 H. Nishida, T. Naoko, Y. Masaji, S. Takaaki and K. Hirsoshi, *Bull. Chem. Soc. Jpn.*, 1984, **57**, 2600–2604.
22 T. Mandai, *ACS Appl. Mater. Interfaces*, 2020, **12**, 39135–39144.
23 W. Ren, D. Wu, Y. NuLi, D. Zhang, Y. Yang, Y. Wang, J. Yang and J. Wang, *ACS Energy Lett.*, 2021, **6**, 3212–3220.
24 K. Tang, A. Du, S. Dong, Z. Cui, X. Liu, C. Lu, J. Zhao, X. Zhou and G. Cui, *Adv. Mater.*, 2020, **32**, 1904987.
25 S. Ha, Y. Lee, S. W. Woo, B. Koo, J. Kim, J. Cho, K. T. Lee and N. Choi, *ACS Appl. Mater. Interfaces*, 2014, **6**, 4063–4073.
26 M. Salama, I. Shterenberg, H. Gizbar, N. N. Eliaz, M. Kosa, K. Keinan-Adamsky, M. Afri, L. J. W. Shimon, H. E. Gottlieb, D. T. Major, Y. Gofer and D. Aurbach, *J. Phys. Chem. C*, 2016, **120**, 19586–19594.
27 J. Eaves-Rathert, K. Moyer, M. Zohair and C. L. Pint, *Joule*, 2020, **4**, 1324–1336.
28 N. N. Rajput, X. Qu, N. Sa, A. K. Burrell and K. A. Persson, *J. Am. Chem. Soc.*, 2015, **137**, 3411–3420.
29 A. Baskin and D. Prendergast, *J. Phys. Chem. C*, 2016, **120**, 3583–3594.
30 N. T. Hahn, E. P. Kamphaus, Y. Chen, V. Murugesan, K. T. Mueller, L. Cheng and K. R. Zavadil, *ACS Appl. Energy Mater.*, 2023, **6**, 3264–3277.
31 Y. Yang, J. Wang, X. Du, H. Jiang, A. Du, X. Ge, N. Li, H. Wang, Y. Zhang, Z. Chen, J. Zhao and G. Cui, *J. Am. Chem. Soc.*, 2023, **145**, 12093–12104.
32 E. W. C. Spotte-Smith, S. M. Blau, D. Barter, N. J. Leon, N. T. Hahn, N. S. Redkar, K. R. Zavadil, C. Liao and K. A. Persson, *J. Am. Chem. Soc.*, 2023, **145**, 12181–12192.
33 S. Hou, X. Ji, K. Gaskell, P. Wang, L. Wang, J. Xu, R. Sun, O. Borodin and C. Wang, *Science*, 2021, **374**, 172–178.
34 W. Zhao, Z. Pan, Y. Zhang, Y. Liu, H. Dou, Y. Shi, Z. Zuo, B. Zhang, J. Chen, X. Zhao and X. Yang, *Angew. Chem., Int. Ed.*, 2022, **134**, e202205187.
35 S. Wang, K. Wang, Y. Zhang, Y. Jie, X. Li, Y. Pan, X. Gao, Q. Nian, R. Cao, Q. Li, S. Jiao and D. Xu, *Angew. Chem., Int. Ed.*, 2023, e202304411.
36 B. D. Adams, J. Zheng, X. Ren, W. Xu and J.-G. Zhang, *Adv. Energy Mater.*, 2018, **8**, 1702097.
37 S. Fan, S. Cora and N. Sa, *ACS Appl. Mater. Interfaces*, 2022, **14**, 46635–46645.
38 Z. Lu, H. Yang, Q. Yang, P. He and H. Zhou, *Angew. Chem., Int. Ed.*, 2022, **61**, e202200410.
39 S. Son, T. Gao, S. P. Harvey, K. X. Steirer, A. Stokes, A. Norman, C. Wang, A. Cresce, K. Xu and C. Ban, *Nat. Chem.*, 2018, **10**, 532–539.
40 Y. Chen, Z. Yu, P. Rudnicki, H. Gong, Z. Huang, S. C. Kim, J. Lai, X. Kong, J. Qin, Y. Cui and Z. Bao, *J. Am. Chem. Soc.*, 2021, **143**, 18703–18713.
41 P. Kubisiak and A. Eilmes, *J. Phys. Chem. C*, 2018, **122**, 12615–12622.
42 S. C. Kim, J. Wang, R. Xu, P. Zhang, Y. Chen, Z. Huang, Y. Yang, Z. Yu, S. T. Oyakhire, W. Zhang, L. C. Greenburg, M. S. Kim, D. T. Boyle, P. Sayavong, Y. Ye, J. Qin, Z. Bao and Y. Cui, *Nat. Energy*, 2023, **8**, 814–826.
43 S. H. Lapidus, N. N. Rajput, X. Qu, K. W. Chapman, K. A. Persson and P. J. Chupas, *Phys. Chem. Chem. Phys.*, 2014, **16**, 21941–21945.
44 W. W. A. van Ekeren, M. Albuquerque, G. Ek, R. Mogensen, W. R. Brant, L. T. Costa, D. Brandell and R. Younesi, *J. Mater. Chem. A*, 2023, **11**, 4111–4125.
45 D. T. Boyle, S. C. Kim, S. T. Oyakhire, R. A. Vilá, Z. Huang, P. Sayavong, J. Qin, Z. Bao and Y. Cui, *J. Am. Chem. Soc.*, 2022, **144**, 20717–20725.
46 Y. Wu, A. Wang, Q. Hu, H. Liang, H. Xu, L. Wang and X. He, *ACS Cent. Sci.*, 2022, **8**, 1290–1298.
47 J. Holoubek, H. Liu, Z. Wu, Y. Yin, X. Xing, G. Cai, S. Yu, H. Zhou, T. A. Pascal, Z. Chen and P. Liu, *Nat. Energy*, 2021, **6**, 303–313.
48 B. Nan, L. Chen, N. D. Rodrigo, O. Borodin, N. Piao, J. Xia, T. Pollard, S. Hou, J. Zhang, X. Ji, J. Xu, X. Zhang, L. Ma, X. He, S. Liu, H. Wan, E. Hu, W. Zhang, K. Xu, X. Yang, B. Lucht and C. Wang, *Angew. Chem., Int. Ed.*, 2022, **61**, e202205967.
49 Y. Chen, R. Atwi, K. S. Han, J. Ryu, N. M. Washton, J. Z. Hu, N. N. Rajput, K. T. Mueller and V. Murugesan, *J. Phys. Chem. B*, 2021, **125**, 12574–12583.
50 C. Fang, B. Lu, G. Pawar, M. Zhang, D. Cheng, S. Chen, M. Ceja, J. Doux, H. Musrock, M. Cai, B. Liaw and Y. S. Meng, *Nat. Energy*, 2021, **6**, 987–994.
51 J. Tang and F. Xu, *Mater. Lett.*, 2020, **320**, 132365.